Journal of Catalysis 269 (2010) 318–328

Contents lists available at ScienceDirect

Journal of Catalysis

journal homepage: www.elsevier.com/locate/jcat

A site-isolated mononuclear iridium complex catalyst supported on MgO: Characterization by spectroscopy and aberration-corrected scanning transmission electron microscopy

Alper Uzun [a], Volkan Ortalan [a], Nigel D. Browning [a,b], Bruce C. Gates [a,*]

[a] Department of Chemical Engineering and Materials Science, University of California, Davis, One Shields Avenue, Davis, CA 95616, USA
[b] Lawrence Livermore National Laboratory, Livermore, CA 94550, USA

ARTICLE INFO

Article history:
Received 28 August 2009
Revised 12 November 2009
Accepted 17 November 2009
Available online 24 December 2009

Keywords:
Scanning transmission electron microscopy
Iridium complex catalyst
Ethene hydrogenation
Single-atom imaging

ABSTRACT

Supported mononuclear iridium complexes with ethene ligands were prepared by the reaction of $Ir(C_2H_4)_2(acac)$ (acac is $CH_3COCHCOCH_3$) with highly dehydroxylated MgO. Characterization of the supported species by extended X-ray absorption fine structure (EXAFS) and infrared (IR) spectroscopies showed that the resultant supported organometallic species were $Ir(C_2H_4)_2$, formed by the dissociation of the acac ligand from $Ir(C_2H_4)_2(acac)$ and bonding of the $Ir(C_2H_4)_2$ species to the MgO surface. Direct evidence of the site-isolation of these mononuclear complexes was obtained by aberration-corrected scanning transmission electron microscopy (STEM); the images demonstrate the presence of the iridium complexes in the absence of any clusters. When the iridium complexes were probed with CO, the resulting IR spectra demonstrated the formation of $Ir(CO)_2$ complexes on the MgO surface. The breadth of the ν_{CO} bands demonstrates a substantial variation in the metal–support bonding, consistent with the heterogeneity of the MgO surface; the STEM images are not sufficient to characterize this heterogeneity. The supported iridium complexes catalyzed ethene hydrogenation at room temperature and atmospheric pressure in a flow reactor, and EXAFS spectra indicated that the mononuclear iridium species remained intact. STEM images of the used catalyst confirmed that almost all of the iridium complexes remained intact, but this method was sensitive enough to detect a small degree of aggregation of the iridium on the support.

1. Introduction

Supported single-site metal complexes are industrial catalysts exemplified by the metallocenes applied for alkene polymerization [1]. When these catalysts are precisely synthesized and structurally well-defined, they are close analogues of molecular metal complexes used in solution catalysis and can in prospect be characterized incisively by a combination of spectroscopic and microscopic methods.

Supported metal complex catalysts are the focus of the research reported herein. Our goal was to investigate a catalyst synthesized precisely from a reactive organometallic precursor, chosen to be $Ir(C_2H_4)_2(acac)$ (acac is acetylacetonate, $CH_3COCHCOCH_3$) [2], because earlier work [3] on the synthesis of a catalyst from this complex on zeolite Y indicates that it adsorbs with the dissociation of the acac ligand and the formation of well-defined $Ir(C_2H_4)_2$ species on the surface. The support was chosen to be MgO because it (a) is composed of atoms that are much lighter than the iridium atoms anchored to it, thus providing a strong contrast in scanning transmission electron microscopy (STEM), (b) is nearly crystalline, offering good images in STEM, and (c) presents surface sites to which the supported metal complex can bond strongly, as on zeolite Y.

A recent communication [4] reports characterization of the MgO-supported iridium complex with atomic-resolution STEM, demonstrating site-isolation of the iridium complexes; infrared (IR) and extended X-ray absorption fine structure (EXAFS) spectra showed that the iridium complex retained its ethene ligands and was bonded to the support via two Ir–O bonds, as on zeolite Y.

Herein we provide a full report on the catalyst synthesis and characterization, evidence of its reactivity in various atmospheres, and a demonstration of its catalytic activity for ethene hydrogenation. Atomic-resolution STEM images of the catalyst before and after it was used for ethene hydrogenation demonstrate the changes occurring during catalysis and indicate the presence of mononuclear iridium complexes as the predominant species.

2. Experimental

2.1. Materials and catalyst synthesis

The catalysts were prepared by the reaction of $Ir(C_2H_4)_2(acac)$ with MgO powder. Sample syntheses and handling were performed

* Corresponding author. Fax: +1 530 752 1031.
E-mail address: bcgates@ucdavis.edu (B.C. Gates).

0021-9517/$ - see front matter © 2009 Published by Elsevier Inc.
doi:10.1016/j.jcat.2009.11.017

with standard air-exclusion methods. The precursor $Ir(C_2H_4)_2$(acac), which has been characterized fully [2], was synthesized as described elsewhere [2]. The MgO support was obtained from EM Science. Hacac (99+%) was obtained from Sigma–Aldrich.

In the synthesis, deionized water was added to the MgO to form a paste, which was dried overnight in air at 120 °C. The resultant solid was ground and treated in flowing O_2 as the temperature was ramped linearly from room temperature to 700 °C and then held for 2 h, resulting in a high degree of dehydroxylation [5]. The treatment in O_2 was immediately followed by evacuation of the sample for 14 h at 700 °C. The resultant calcined MgO was cooled to room temperature under vacuum [6]. The surface area of final product was approximately 100 m^2/g.

To prepare the supported catalyst containing 1.0 wt.% Ir, the precursor $Ir(C_2H_4)_2$(acac) (54 mg) and calcined MgO (2.946 g) were slurried in dried and deoxygenated *n*-pentane (Fisher, 99%) that was initially at dry-ice temperature. The slurry was kept at this temperature for 2 days of mixing, and thereafter the solvent was removed by evacuation for a day. The resultant supported catalyst was light gray in color. It was stored in an argon-filled glove box (<1 ppm O_2 and <1 ppm H_2O).

In another preparation, to make a sample for comparison with the catalyst and to help determine how the acac groups on $Ir(C_2H_4)_2$(acac) reacted in the catalyst preparation, the reaction of Hacac with calcined MgO was carried out in *n*-pentane with exclusion of air and moisture; the slurry was stirred for one day, and the solvent was removed by evacuation for one day.

H_2 used for treating the catalyst and as a reactant in ethene hydrogenation catalysis was supplied by Airgas (99.999%) or generated by electrolysis of water in a Balston generator (99.99%). It was purified by passage through traps containing particles of reduced Cu/Al_2O_3 and activated zeolite 4A to remove traces of O_2 and moisture, respectively. Helium (Airgas, 99.999%), C_2H_4 (Airgas, 99.99%), and CO (10% in helium) were purified by passage through similar traps. The corresponding pressures of each treatment are given in appropriate sections below.

2.2. Ethene hydrogenation catalysis in a tubular plug-flow reactor

Ethene hydrogenation catalysis was carried out in a conventional laboratory once-through flow reactor well approximated as a plug-flow reactor. The catalyst powder (100 mg) diluted with particles of inert, nonporous α-Al_2O_3 in a mass ratio of Al_2O_3 to catalyst of 30:1 was loaded into the reactor in the argon-filled glove box. The reactor was then sealed inside the glove box with quick connectors and was transferred to the flow system for operation at atmospheric pressure. The feed ethene and H_2 partial pressures were 40 mbar each, and the temperature was 25 ± 1 °C. Details of the reaction experiments and product analysis by gas chromatography are as described elsewhere [3]. Conversions of ethene to ethane were <5%, and the reactor operated in the differential mode, determining the reaction rates directly.

2.3. IR spectroscopy

A Bruker IFS 66v/S spectrometer with a spectral resolution of 2 cm^{-1} was used to collect transmission spectra of powder catalyst samples. In an argon-filled glove box, approximately 10 mg of each sample was pressed between two KBr windows for optical optimization that allowed detection of minor peaks. IR spectra were recorded with samples, handled with exclusion of moisture and air, at room temperature under vacuum, with an average of 128 scans per spectrum.

In some experiments, the catalyst was present in a cell with reactive gases flowing through it. In these experiments, each sample (typically, 10 mg) was pressed into a thin wafer and loaded into the cell (In-situ Research Institute, Inc., South Bend, IN) in the argon-filled glove box. The cell was then transferred and connected quickly to a flow system, which allowed recording of spectra while the reactant and/or inert gas (CO, H_2, He, or $H_2 + C_2H_4$) flowed through the cell at the reaction temperature. In some experiments, pulses of CO in helium flowed through the cell; each pulse consisted of 5 mL of CO (10 vol% in helium) flowing at 100 mL/min. Each spectrum is the average of 64 scans.

2.4. Mass spectrometry of effluent gases

Mass spectra of the gases introduced into the flow system and the effluents produced by reaction with the catalyst in the IR cell were measured with an online Balzers OmniStar mass spectrometer running in multi-ion monitoring mode; the mass spectra were recorded simultaneously with the IR spectra of the solid catalyst. Changes in the signal intensities of the major fragments of C_2H_4 (m/z = 26, 27, and 28), C_2H_6 (m/z = 26, 27, 28, and 30), and CO (m/z = 28) were recorded in transient experiments.

2.5. Scanning transmission electron microscopy

High-angle annular dark-field (HAADF) STEM images of fresh and used catalysts were obtained with a FEI Titan electron microscope equipped with a high-brightness field emission gun and operated at 300 kV with a CEOS dodecapole probe (STEM) aberration corrector. The microscope was located at the SHaRE Facility of the Oak Ridge National Laboratory (ORNL).

Extreme care was taken to minimize exposure of the catalysts to air and to minimize the sample degradation that would result. Thus, samples of the unused catalyst were transferred with air exclusion to a glove box filled with ultrahigh-purity argon, where they were placed in a stainless-steel tube sealed with vacuum flanges. These samples were then transported to ORNL, where they were removed from the tube in a glove bag purged with ultrahigh-purity argon. In the glove bag, each sample was loaded onto a lacey carbon grid, which was inserted in a TEM holder. The glove bag was placed next to the microscope, and the TEM holder was transferred in less than 3 s into the microscope. The turbo-molecular pump evacuating the microscope chamber was switched on several minutes before insertion of the sample so that it could come up to operational speed, allowing rapid evacuation of the chamber. Once the specimen had been inserted, the evacuation of the airlock was begun immediately; nonetheless, there was a period of <5 s during which traces of air might have intruded into the sample prior to its insertion into the airlock and re-establishment of the vacuum. (To evaluate the effect of such contact, we tested the catalyst by measuring the IR spectra after exposing it to air for even longer times (up to 10 s); the spectra demonstrate the lack of any measurable changes resulting from the exposure.)

Samples of used catalyst were prepared for imaging by purging the flow reactor with flowing helium for 2 h to remove any weakly adsorbed species. Then the sample was handled the same way as fresh samples for STEM imaging.

The probe size of the microscope was approximately 0.8 Å (determined from the simulated probe using the following parameters: 300 kV, C3 = −0.01 mm, C5 = 5 mm at Gaussian defocus).

The contrast in an HAADF image is formed by mapping the intensity of high-angle scattered electrons as the probe is scanned across the specimen. High-angle scattering arises predominantly from the atomic nuclei (Rutherford scattering); therefore, the image is incoherent, and the scattering cross section depends on the atomic number (Z) squared. As a result, Z-contrast images exhibit weak dependence on sample thickness and a strong chemical sensitivity (dependence on Z^2). Therefore, it is possible to image

heavy single atoms (Ir, $Z = 77$) on a light support (Mg, $Z = 12$; O, $Z = 8$), even in relatively thick specimens (~500 Å).

2.6. X-ray absorption spectroscopy (XAS)

EXAFS spectra were collected at beamline X-18B at the National Synchrotron Light Source (NSLS), Brookhaven National Laboratory, and at beamline 10-2 at the Stanford Synchrotron Radiation Laboratory (SSRL), Stanford Linear Accelerator Center. The storage ring electron energy was 2.8 GeV at NSLS and 3.0 GeV at SSRL. The ring currents were 110–250 mA and 50–100 mA at NSLS and SSRL, respectively.

In an argon-filled glove box at NSLS or a N_2-filled glove box at SSRL, each powder sample was loaded into an EXAFS cell [7]. The cell was evacuated to a pressure less than 1.3×10^{-5} mbar and aligned in the X-ray beam. Spectra were then collected in transmission mode at the Ir L_{III} edge (11215 eV) with the sample cooled to approximately liquid–nitrogen temperature. In some experiments, spectra were collected with the sample at 25 °C during treatment in flowing helium, C_2H_4, H_2, or $H_2 + C_2H_4$ in an EXAFS cell like that described elsewhere [8].

For measurements of a sample working as an ethene hydrogenation catalyst, the sample was initially scanned in flowing helium, and then the feed stream composition was switched to a mixture of H_2 + ethene (40 mbar each, with the remainder being helium and the pressure atmospheric). After the measurement of an initial EXAFS spectrum, the steady flow of reactants continued for 2 h as XANES spectra were collected, followed by the recording of four EXAFS spectra at the end of the experiment.

3. EXAFS data analysis

The X-ray absorption edge energy was calibrated with the measured signal of iridium metal powder at the Ir L_{III} edge (11,215 eV); this foil was scanned simultaneously with the sample. Ir L_{III} EXAFS data were collected at energies near that of the edge (11,215 eV). The data were normalized by dividing the absorption intensity by the height of the absorption edge.

Analysis of the EXAFS data was carried out with the software ATHENA (part of the IFEFFIT package) [9] and the software XDAP [10]. Athena was used for data alignment, edge calibration, and deglitching. Data normalization, background subtraction, and conversion of the data into a chi file and data fitting were performed with XDAP [10], which allows the efficient application of a difference-file technique [11–13] for the determination of optimized fit parameters and isolation of individual shells.

Reference files used in the data analysis were calculated with the code FEFF7.0 [14]. The Ir–Ir and Ir–Mg phase shifts and backscattering amplitudes were calculated from the structural parameters characterizing iridium metal and $IrMg_3$, respectively. The crystal structure of $Ir(C_2H_4)_2(acac)$ [2] was used to calculate the phase shifts and backscattering amplitudes representing the Ir–C and Ir–O shells, because it was expected that the structure of the supported iridium species would be similar to that of this precursor.

Iterative data fitting was carried out for various structural models of the supported iridium complex until the best agreement was attained between the calculated k^0-, k^1-, and k^2-weighted EXAFS data and the postulated model (k is the wave vector). The models included the following contributions (Table 1): Ir–O, Ir–C, Ir–Mg, and Ir–O_l (Ir–O_l is a long Ir–O distance, that is, longer than an Ir–O bonding distance). These contributions were chosen for the EXAFS data fitting because they were all expected on the basis of reports of similar supported organometallic complexes [3,6,15]; specifically, the literature [3,6,15] indicates the likelihood of formation of bonds between Ir atoms and support oxygen atoms, which implies the presence of Ir–O, Ir–Mg, and Ir–O_l contributions. Furthermore, the presence of hydrocarbon ligands on the iridium (corresponding to an Ir–C contribution in the EXAFS spectrum) was indicated by the υ_{CH} bands in the IR spectra (Fig. 1).

In the EXAFS data fitting, more than one statistically justifiable model was obtained to characterize the structure of the catalyst before operation (and after operation for the ethene hydrogenation for 2 h). To select the recommended model in each case, we compared the various candidate models with respect to the physical appropriateness of each parameter in each model and their goodness of fit values (the smaller the goodness of fit values, the better the fit), as summarized in Tables 2 and 3. We emphasize that attempts were made to include Ir–Ir contributions in all of the models, but none was found (even with a k^3 weighting of the data), and that it was difficult to distinguish Ir–Mg and long Ir–O contributions from each other. Thus, the Ir–Mg and/or long Ir–O contributions are assigned only tentatively, and the errors characterizing such shells are greater than those stated below for other shells. A part of the challenge of analyzing these shells is obtaining suitable references as a basis for approximating the structure of the Ir support interface [3].

In the analysis of the data characterizing the unused catalyst, the fitting ranges in both momentum (k) and real (r) space (r is distance from the absorbing Ir atom) were determined by the data quality. The range in k was 2.9–12.0 $Å^{-1}$, and the range in r was 1.0–3.8 Å. These values were used with the Nyquist theorem [16] to estimate the justified number of fitting parameters. The number of parameters used in fitting the data to each model (16) was always less than this number (approximately 18).

Table 1
EXAFS parameters[a] characterizing MgO-supported iridium complex catalyst at 298 K before and after 2 h of operation in a flow reactor for ethene hydrogenation.

Composition of gas in contact with sample	Absorber–backscatterer pair	N	R (Å)	$10^3 \times \Delta\sigma^2$ ($Å^2$)	ΔE_0 (eV)
Helium	Ir–Ir	[b]	[b]	[b]	[b]
	Ir–C	3.9	2.11	1.7	−6.5
	Ir–O	2.0	2.15	0.8	2.8
	Ir–Mg	2.8	3.05	11.1	−2.1
	Ir–O_l	4.5	3.73	10.9	−4.1
$C_2H_4 + H_2$ + He (during catalytic ethene hydrogenation after 2 h on stream)	Ir–Ir	[b]	[b]	[b]	[b]
	Ir–C	3.8	2.05	0.8	−5.7
	Ir–O	2.1	2.13	0.7	6.3
	Ir–Mg	2.7	2.96	8.6	6.7
	Ir–O_l	3.4	3.70	1.7	3.0

[a] Ir–O_l represents long iridium–oxygen contributions, characterizing interaction of Ir atoms with the neighboring non-bonding O atoms. Error bounds (accuracies) characterizing the structural parameters obtained by EXAFS spectroscopy are estimated to be as follows: coordination number N, ±20%; distance R, ±0.02 Å; Debye–Waller factor $\Delta\sigma^2$, ±20%; and inner potential correction ΔE_0, ±20% (also see text).
[b] Contribution undetectable.

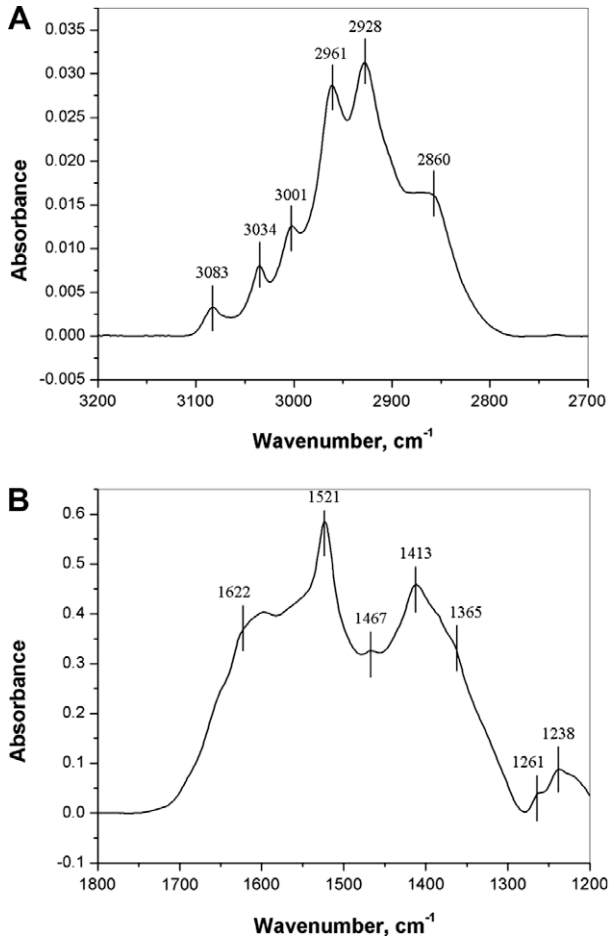

Fig. 1. IR spectra characterizing the unused catalysts formed by the reaction of MgO (calcined at 700 °C) with $Ir(C_2H_4)_2(acac)$ in *n*-pentane after the removal of the solvent: (A) in the υ_{CH} region characterizing the ethene ligands and (B) in the region of 1200–1800 cm^{-1} characterizing the bands corresponding to acac ligands.

In the analysis of the data characterizing the sample during the catalytic reaction of ethene with H_2 at 25 °C, the fitting range in *k* space was 2.8–13.2 $Å^{-1}$, and the range in *r* space was 1.0–3.8 Å. Again, the number of parameters used in the fitting (16) was always less than that estimated by the Nyquist theorem with these ranges (approximately 21).

The accuracies of the parameters are estimated to be as follows (with the exception of the Ir–Mg and longer Ir–O contributions): coordination number *N*, ±10%; distance *R*, ±0.02 Å; Debye–Waller factor $\Delta\sigma^2$, ±20%; and inner potential correction ΔE_0, ±20%.

Further details of the EXAFS analysis are essentially the same as those reported elsewhere [3].

4. Results

4.1. Characterization of unused catalyst

4.1.1. Spectroscopic evidence of iridium diethene complexes

During the preparation of the catalyst by the reaction of $Ir(C_2H_4)_2(acac)$ with highly dehydroxylated MgO, the *n*-pentane solvent that was used to deliver the precursor to the MgO became colorless, indicative of nearly complete uptake of the precursor by the support. When the solvent was later removed by evacuation, all of the iridium remained on the MgO. The preparation conditions were chosen to give an iridium loading of 1.0 wt.% as described in Section 2.1.

IR data characterizing the sample prepared by the adsorption of $Ir(C_2H_4)_2(acac)$ on the MgO are shown in Fig. 1 and Table 4. The spectra include bands in the C–H stretching region (3200–2800 cm^{-1}) and the region where bands characteristic of acac ligands are expected (1800–1200 cm^{-1}). We interpret the spectra as evidence of chemisorption of the $Ir(C_2H_4)_2(acac)$ on MgO, as follows:

The IR bands at 3034 and 3001 cm^{-1} are assigned to υ_{CH} bands of π-bonded ethene in the supported iridium complex, approximately matching those of the precursor $Ir(C_2H_4)_2(acac)$ (3045 and 2981 cm^{-1}) [2,3]. Other bands in the spectra characterizing the supported iridium complex (Fig. 1 and Table 4) were observed at 3083, 2961, 2928, 2860, 1622, 1521, 1467, 1413, 1365, 1261, and 1238 cm^{-1}, and these approximately match a set of bands in the spectra characterizing $Mg(acac)_2$ (at 2993, 2970, 2925, 1625, 1528, 1489, 1423, 1371, 1263, and 1199 cm^{-1}) and Hacac adsorbed on MgO (at 2993, 2965, 2920, 1620, 1521, 1465, 1418, 1367, 1265, and 1199 cm^{-1}) [6]. This comparison suggests that the acac ligand present in $Ir(C_2H_4)_2(acac)$ was dissociated from the iridium and chemisorbed on the MgO during the chemisorption. Similar results have been reported for supported catalysts prepared by the reaction of $Rh(C_2H_4)_2(acac)$ [6] with MgO and $Au(CH_3)_2(acac)$ with MgO [15], as well as for the reaction of $Ir(C_2H_4)_2(acac)$ with highly dealuminated zeolite HY [3].

Further evidence of the supported iridium complex is provided by the EXAFS data (Fig. 2); the parameters obtained by fitting the

Table 2
Summary of EXAFS fit parameters[a,b] for each of the candidate fit models (I, II, and III) characterizing the structure of MgO-supported iridium complex formed from the reaction of $Ir(C_2H_4)_2(acac)$ with highly dehydroxylated MgO.

Model	Absorber–backscatterer contribution	*N*	*R* (Å)	$10^3 \times \Delta\sigma^2$ ($Å^2$)	ΔE_0 (eV)
I	Ir–C	3.9	2.11	1.7	−6.5
	Ir–O	2.0	2.15	0.8	2.8
	Ir–Mg	2.8	3.05	11.1	−2.1
	Ir-O_l	4.5	3.73	10.9	−4.1
II	Ir–C	3.7	2.03	10.4	−11.0
	Ir–O	4.1	2.05	8.4	6.5
	Ir–Mg	2.2	3.09	10.7	−4.5
	Ir-O_l	4.9	4.00	10.6	8.0
III	Ir–C	2.1	2.05	1.8	1.5
	Ir–O	0.9	2.19	1.3	−18.1
	Ir–Mg	1.6	3.10	7.6	−8.9
	Ir-O_l	2.5	3.73	5.9	−2.9

[a] *Notation: N*, coordination number; *R*, distance between absorber and backscatterer atoms; $\Delta\sigma^2$, Debye–Waller factor; ΔE_0, inner potential correction. Error bounds (accuracies) characterizing the structural parameters obtained by EXAFS spectroscopy are estimated to be as follows: coordination number *N*, ±20%; distance *R*, ±0.02 Å; Debye–Waller factor $\Delta\sigma^2$, ±20%; and inner potential correction ΔE_0, ±20.

[b] Ir–O_l is an Ir–O contribution with a distance longer than a bonding distance.

Table 3
Qualitative summary of EXAFS fitting results with fit diagnostic parameters for three candidate models characterizing the structure of MgO-supported iridium complex formed from the reaction of $Ir(C_2H_4)_2(acac)$ with highly dehydroxylated MgO.

Model	Absorber–backscatterer contributions	Comments regarding the quality of fit of EXAFS data	Error in EXAFS function, χ[a]	Goodness of fit[b]
I	Ir–C Ir–O Ir–Mg Ir–O_l	Good overall fit (as shown by goodness of fit parameter). Good individual fits for all contributions. Physically realistic values of all fit parameters	0.002	7.1
II	Ir–C Ir–O Ir–Mg Ir–O_l	Adequate overall fit; however, poor fits of individual contributions (especially when the phase- and amplitude-correction is applied). Physically unrealistic values of the fit parameters: Unrealistic coordination numbers for Ir–O contribution, and ΔE_0 value	0.002	6.8
III	Ir–C Ir–O Ir–Mg Ir–O_l	Adequate overall fit; however, poor fits of individual contributions (especially when the phase- and amplitude-correction is applied). Physically unrealistic values of the fit parameters: Unrealistic coordination numbers for Ir–O contribution, and ΔE_0 value and poor fit for the long Ir–O shell	0.002	12.5

[a] The error in data was calculated by the root mean square of the value obtained from the subtraction of smoothed χ data from the background-subtracted experimental χ values.
[b] Goodness of fit values were calculated with the software XDAP, as follows:

$$\text{goodness of fit} = \frac{v}{NPTS(v - N_{\text{free}})}\sum_{i=1}^{\text{NPTS}}\left(\frac{\chi_{\text{exp}} - \chi_{\text{model}}}{\sigma_{\text{exp}}}\right)^2.$$

The terms χ_{model} and χ_{exp} are the model and experimental EXAFS values, respectively; σ_{exp} is the error in the experimental results; v is the number of independent data points in the fit range; and NPTS is the actual number of data points in the fit range; N_{free} is the number of free parameters.

Table 4
Frequencies of IR bands observed in C–H stretching region and in acetylacetonate region characterizing reference compounds and sample formed by adsorption of $Ir(C_2H_4)_2(acac)$ on highly dehydroxylated MgO.

Sample				Assignment
$Mg(acac)_2$	Hacac/MgO	$Ir(C_2H_4)_2(acac)$	$Ir(C_2H_4)_2$ on MgO	
3128	–	–	3083	Not assigned
–	–	3045	–	$\upsilon(CH_2)$ (π-bonded ethene)
–	–	3030	3034	$\upsilon(CH_2)$ (π-bonded ethene)
–	–	2981	3001	$\upsilon(CH_2)$ (π-bonded ethene)
2993	2993	–	–	$\upsilon(CH_3)$ (acac)
2970	2965	2935	2961	$\upsilon(CH_3)$ (acac)
2925	2920	2906	2928	$\upsilon(CH_3)$ (acac)
2866	–	2879	2860	Not assigned
1623	1620	1576	1622	υ(C–C) {or υ(C–O)}
1528	1521	1549	1521	υ(C–O) {or υ(C–C)}
1489	1465	1486	1467	υ(C–C) + δ(C–H)
1423	1418	1424	1413	$\delta_d(CH_3)$
1371	1367	1361	1365	$\delta_s(CH_3)$
1263	1265	1276	1261	υ_s(C–C) + υ(C–CH_3)
1199	1199	1212	1238	υ_s(C–CH_3) + δ(C–H)

data are summarized in Table 1. We re-emphasize that the data give no indication of Ir–Ir contributions (for any of the fit models considered), consistent with the presence of site-isolated mononuclear iridium complexes in the absence of clusters detectable by EXAFS spectroscopy. Furthermore, the Ir–C contribution in the EXAFS spectrum, with a coordination number of 4.0 at a distance of 2.06 Å, confirms the IR evidence of ethene ligands and indicates two π-bonded ethene ligands per Ir atom. The Ir–O contribution characterizing the metal–support interface (Table 1) shows that on average, each Ir atom was bonded to the support via two oxygen atoms at a distance of 2.15 ± 0.02 Å, which is a typical bonding distance for group-8 metal complexes [6] and metal clusters on oxide supports [17]; for example, the Rh–O distance found by EXAFS spectroscopy for the isostructural $Rh(C_2H_4)_2$ complex on MgO (formed from $Rh(C_2H_4)_2(acac)$) was 2.18 ± 0.02 Å [6], and that for the similar $Ir(C_2H_4)_2$ complex bonded to dealuminated HY zeolite was 2.17 ± 0.02 Å [3]. These distances are significantly different from the Ir–O bonding distance in crystalline $Ir(C_2H_4)_2(acac)$ (2.04 Å) [2], consistent with the inference that the acac ligands were removed from the iridium in the adsorption process and that the iridium became bonded to oxygen atoms of the MgO surface rather than acac ligands.

XANES spectra (Fig. 3) show that the edge position of the freshly prepared sample is approximately 2 eV higher in energy than that of the iridium metal powder. This comparison indicates the presence of cationic iridium, as in the precursor $Ir(C_2H_4)_2(acac)$, which is formally an Ir(I) complex incorporating the bidentate acac ligand [2]. The edge position rules out a detectable amount of zerovalent iridium in the supported sample—and thus rules out a substantial number of iridium particles.

4.1.2. STEM evidence of site-isolation of MgO-supported iridium complexes

The STEM images provide evidence of well-separated mononuclear iridium complexes on the MgO—in the absence of detectable iridium clusters, as shown by a comparison of the STEM images of the unused catalyst (Fig. 4) and that of the MgO support alone, after dehydroxylation, as follows: Fig. 4 is a typical image of the catalyst,

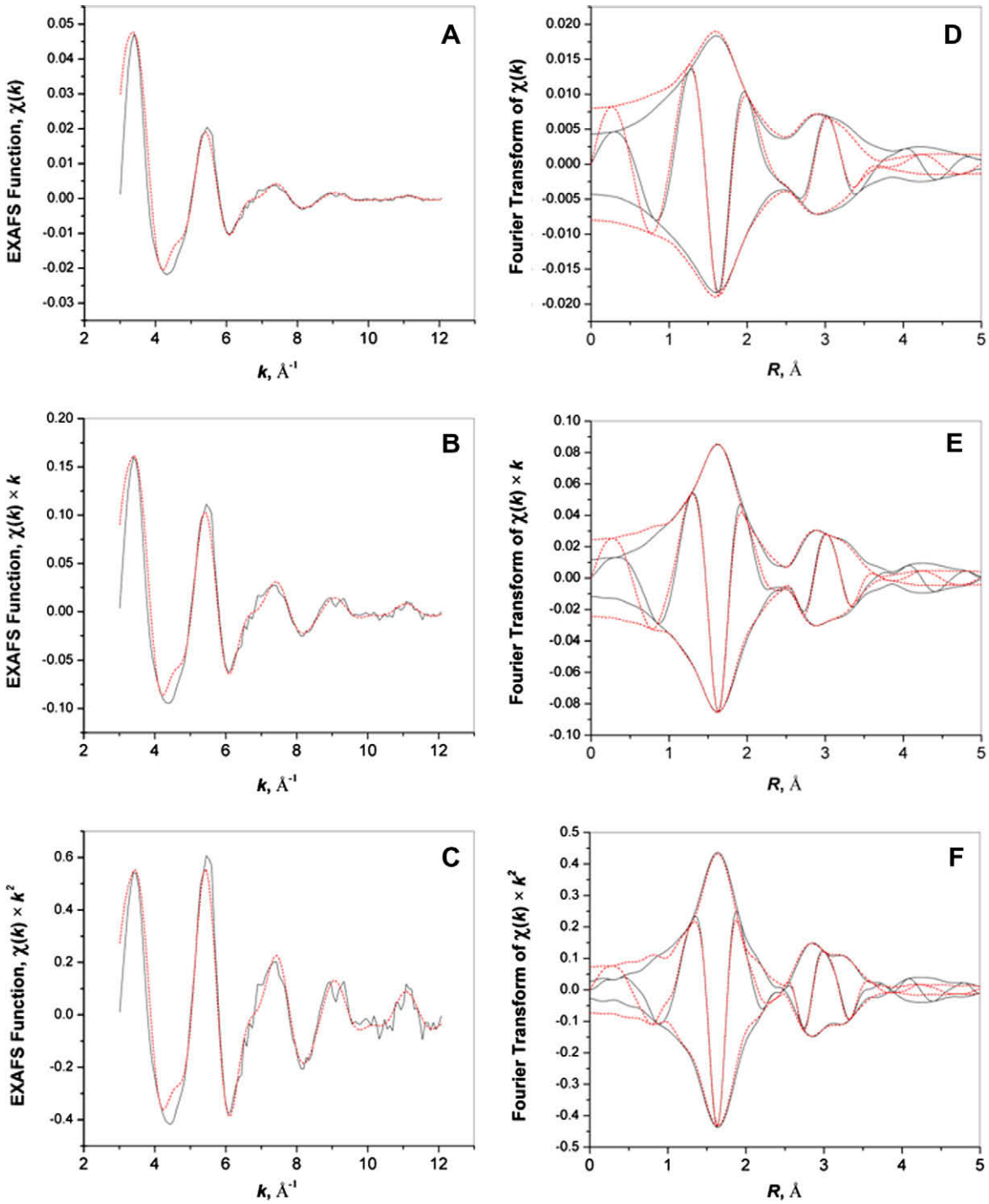

Fig. 2. Results of EXAFS analysis characterizing the sample formed by the reaction of $Ir(C_2H_4)_2(acac)$ with MgO that had been calcined at 700 °C. EXAFS function, χ (solid black line), and calculated contribution (dotted red line): (A) k^1-weighted; (B) k^2-weighted; and (C) k^3-weighted. Imaginary part and magnitude of the Fourier transform of data (solid black lines) and calculated contributions (dotted red lines): (D) k^1-weighted; (E) k^2-weighted; and (F) k^3-weighted (Δk = 3.0–12.1 Å^{-1}). (For interpretation of the references to color in this figure legend, the reader is referred to the web version of this article.)

clearly indicating site-isolated Ir atoms on the MgO; individual Ir atoms are indicated by the bright scattering centers. These scattering centers are not evident in the images of blank samples which consist of the pure highly dehydroxylated MgO alone (not shown).

Because both Mg and O are light atoms, and the thickness of the support cannot be determined from the images, it was not possible to find STEM evidence of any defect sites on the MgO surface; thus we cannot report any insights regarding the bonding sites for the Ir atoms on the basis of the images.

The image shown in Fig. 4 provides clear evidence of the surface of a nearly planar part of a single MgO crystal. Where Ir atoms are evident on this surface, the loading calculated from the image is approximately one-third of that of the sample as a whole.

This demonstration of single-Ir-atom complexes on the MgO is consistent with the IR and EXAFS spectra (Tables 1 and 4) indicating the presence of mononuclear iridium complexes with π-bonded ethene ligands. This STEM result, which has been commu-

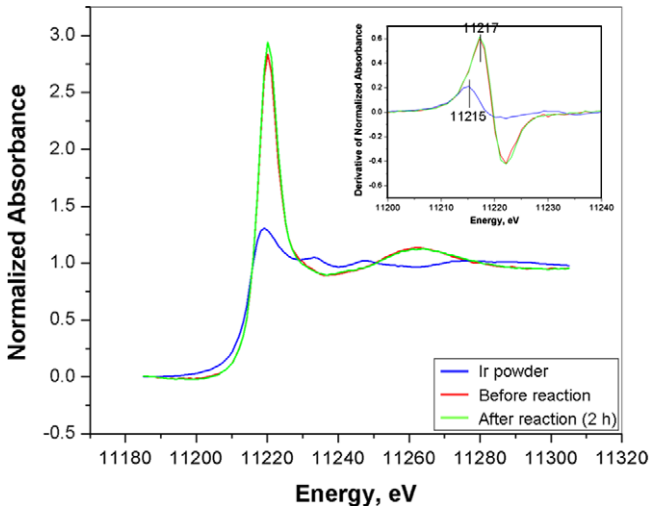

Fig. 3. Normalized XANES spectra at the Ir L_{III} edge characterizing the catalyst formed from $Ir(C_2H_4)_2(acac)$ and MgO before and after reaction in equimolar ethene and H_2 at 25 °C and atmospheric pressure. For comparison, the spectrum of iridium powder is also shown. The inset indicates the derivatives of spectra illustrating the energy edge positions. (For interpretation to colors in this figure, the reader is referred to the web version of this paper.)

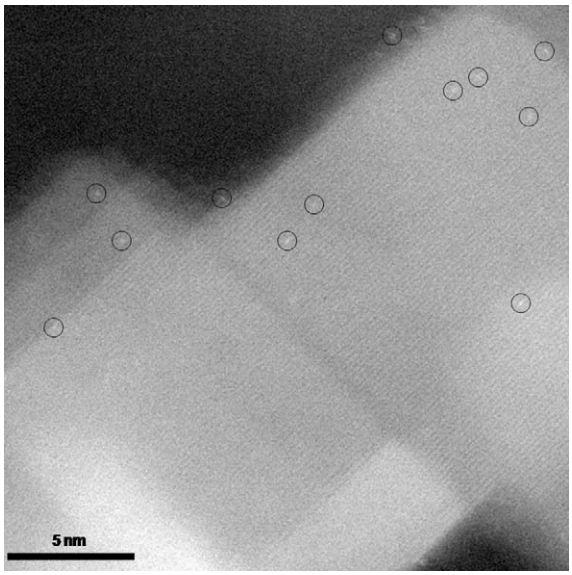

Fig. 4. High-angle annular dark-field (*Z*-contrast) image characterizing the unused catalyst prepared by the reaction of $Ir(C_2H_4)_2(acac)$ with highly dehydroxylated MgO that had been calcined at 700 °C. The image shows individual Ir atoms as bright scattering centers (indicated by black circles), which are well dispersed and present in the absence of detectable iridium clusters.

nicated [4], is the first demonstration of the site-isolation of mononuclear metal complexes bonded to a high-area support.

We emphasize that the conclusions drawn here from STEM images are based only on images that were the first obtained in any region of the sample, because subsequent images clearly demonstrate the effects of the electron beam, which caused migration of the Ir atoms (possibly facilitated by modification of the ligands), formation of iridium clusters, and even subsequent breakup of the resultant clusters into smaller clusters.

Some parts of the sample had higher loadings of Ir atoms than that shown in Fig. 4, and the effects of the electron beam on the iridium in the zones of high loading were more pronounced than those pertaining to the region shown in Fig. 4. Comparable electron beam damage of highly dispersed supported metals has been reported previously [18–21].

4.2. Reactivity of MgO-supported iridium complexes in various gas atmospheres

The reactivities of the supported iridium diethene complexes under various conditions were characterized by IR and EXAFS spectra of samples in flow-through cells and by mass spectrometric analysis of the effluent gas stream.

4.2.1. Reaction of MgO-supported iridium diethene complexes with CO

The surface-bound $Ir(C_2H_4)_2$ species were probed with a pulse of CO injected into a helium stream flowing into the IR cell. The surface species formed by the exchange were characterized by IR spectroscopy, as follows: in a preliminary treatment, the surface-bound $Ir(C_2H_4)_2$ was treated in flowing helium for 1 h to purge any weakly absorbed species from the sample. Then a CO pulse was injected as the recording of IR spectra continued. The spectra demonstrate the almost instantaneous formation of two bands in the ν_{CO} region, at 2066 and 1985 cm^{-1}, accompanied by the disappearance of the bands associated with π-bonded ethene ligands (at 3034 and 3001 cm^{-1}) (Fig. 5). These newly formed bands are assigned straightforwardly to the well-known iridium *gem*-dicarbonyl $Ir(CO)_2$ [3,22–24]. Thus, we infer that CO readily replaced the π-bonded ethene ligands. Correspondingly, the mass spectra of the effluent gas swept from the IR cell gave evidence of ethene fragments and ethane fragments (indicated by $m/z = 26$, 27, and 30, Supplementary material). Similar chemistry has been observed with (a) iridium diethene complexes bonded to dealuminated HY zeolite, for which the newly formed ν_{CO} bands were located at 2109 and 2038 cm^{-1} [3], and (b) the isostructural rhodium complexes bonded to MgO indicated by bands formed at 2082 and 2004 cm^{-1} after the introduction of CO [6].

The full width at half maximum (fwhm) of each of the ν_{CO} bands of $Ir(CO)_2$ was approximately 26 cm^{-1}, which is markedly greater than what was observed with the iridium complexes bonded to the dealuminated zeolite (approximately 5 cm^{-1}) [3,25]. We infer that because of the nonuniformity of the MgO support surface, the ligand environments of the iridium carbonyls on MgO varied from site to site, leading to the breadth of the IR bands. Thus, we emphasize that the iridium complexes on MgO were not as uniform as those observed on the zeolite [3]. Therefore, we infer that although the STEM images demonstrate the site-isolation of the iridium complexes and their uniform mononuclearity on the crystalline part of the MgO, the bonding of these complexes to the support lacks a high degree of uniformity.

4.2.2. Reaction of MgO-supported iridium diethene complexes with H_2

When the unused catalyst was treated in flowing H_2 at 25 °C and atmospheric pressure in the IR cell/flow reactor, spectra were observed that demonstrate the decrease in intensity of the bands at 3034 and 3001 cm^{-1} (characteristic of the π-bonded ethene ligands) and the simultaneous formation of new bands at 2965, 2929, 2876, and 2860 cm^{-1} (Fig. 6). These new bands are assigned to ethyl ligands, as before [26–28]. Thus, the spectra indicate that the π-bonded ethene ligands reacted with H_2 to form ethyl ligands suggesting a step that might be important in ethene hydrogenation catalysis, because both π-bonded ethene and ethyl ligands are known intermediates in this reaction [3,26].

When the sample was in the presence of H_2 at higher temperatures, the iridium underwent aggregation into particles, as expected for this group-8 metal on the basis of earlier results characterizing the formation of iridium particles during the treatment of Al_2O_3-supported $Ir_4(CO)_{12}$ at 500 °C in flowing H_2. The

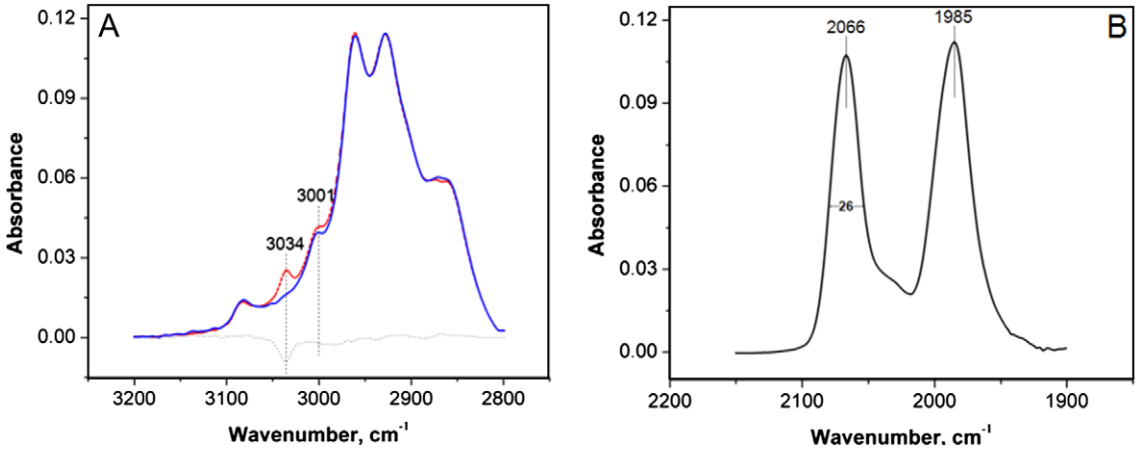

Fig. 5. IR spectra characterizing CO exchange with ethene during the CO treatment of the catalyst formed by chemisorption of $Ir(C_2H_4)_2(acac)$ on highly dehydroxylated MgO: (A) change in υ_{CH} region (red line: unused catalyst; blue line: after CO treatment) and (B) change in υ_{CO} region. (For interpretation of the references to colors in this figure legend, the reader is referred to the web version of this paper.)

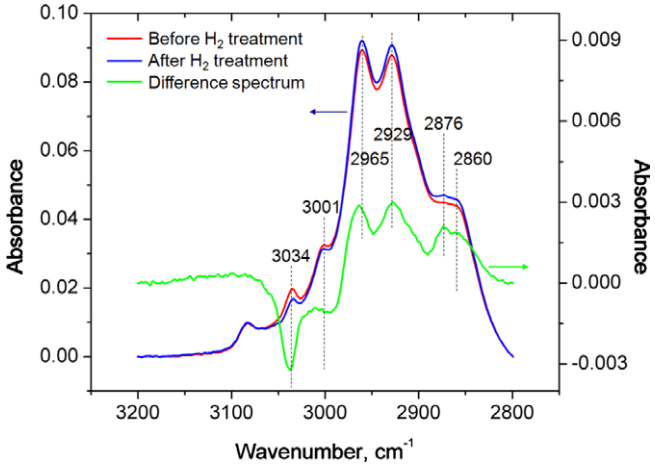

Fig. 6. IR spectra in the υ_{CH} region characterizing catalysts prepared by the chemisorption of $Ir(C_2H_4)_2(acac)$ on highly dehydroxylated MgO after it had been treated in flowing H_2 for 2 h: Red line: unused catalyst; blue line: after H_2 treatment; green line: difference spectrum obtained by subtracting the spectrum of the fresh catalyst from that of the treated catalyst. (For interpretation of the references to color in this figure legend, the reader is referred to the web version of this article.)

Ir–Ir coordination number in the resultant structure was found to be approximately 9, indicating the formation of particles large enough to be essentially metallic [29].

4.3. Ethene hydrogenation catalyzed by MgO-supported iridium complexes

Consistent with the IR results identifying the formation of ethyl ligands when the catalyst was in contact with H_2, the MgO-supported iridium complex catalyzed ethene hydrogenation in a once-through flow reactor under the conditions stated above. The data show that ethene conversion decreased from an initial value of approximately 15% to approximately 1% during a break-in period of 60 min, consistent with changes in the ligand environment of the iridium. (The ligands on the iridium initially were ethene, as shown by the IR and EXAFS results; therefore, the initial conversion value of 15% was only apparent, including the contribution of ethane formed from these initially present ethene ligands. Thereafter, the catalyst operated at near steady state at a conversion of 1% (Supplementary material). The catalyst did not show significant deactivation during a subsequent 24-h period of operation in the flow reactor. Thus, a steady-state turnover frequency (TOF) was calculated by assuming that each Ir atom was part of a catalytically active species; the TOF value was 4.7×10^{-3} ethene molecules $\times$ (Ir atom $\times$ s)$^{-1}$. There was no detectable activity in the absence of the catalyst, and the MgO support alone was inactive. Therefore, we infer that the catalytic activity is attributable to the iridium species on the MgO.

4.4. Characterization of used catalyst

4.4.1. Spectroscopic evidence of intact MgO-supported iridium complex after use for ethene hydrogenation

4.4.1.1. XAS results characterizing nuclearity of iridium species. The EXAFS results characterizing the catalyst after 2 h of operation under the conditions stated above give no evidence of Ir–Ir contributions, demonstrating that mononuclear iridium complexes were the predominant species in the catalyst. As in the case of the unused catalyst, the Ir–O coordination number representing the bonding between the Ir atoms and the support was found to be approximately 2.1 ± 0.4 (it was found to be 2.0 ± 0.4 for the unused catalyst) with a bonding distance of 2.13 ± 0.02 Å (the corresponding value was 2.15 ± 0.02 Å for the unused catalyst), consistent with the lack of any aggregation of the iridium (one would expect a decrease in the average Ir–O coordination number when clusters formed). Moreover, XANES spectra recorded during the operation of the catalyst as it approached steady state show a small increase in the white-line intensity at the Ir L_{III} edge but almost no change in the edge energy relative to the value characterizing the sample in the initial state in helium (Fig. 3). These observations are consistent with the lack of significant aggregation of the iridium and point to changes in the ligand environment of the iridium as the catalyst approached steady-state operation.

4.4.1.2. IR spectra providing evidence of mononuclear iridium species. IR data obtained by probing the catalyst with a pulse of CO following the ethene hydrogenation in the flow reactor after attainment of steady state (demonstrated by the mass spectrometric analysis of the catalytic reaction products) under the conditions stated above for the unused catalyst indicate the formation of the bands assigned to the iridium *gem*-dicarbonyl, $Ir(CO)_2$ (at 2066 and 1985 cm^{-1}), confirming the presence of mononuclear iridium complexes, we infer, before the injection of CO (Fig. 7).

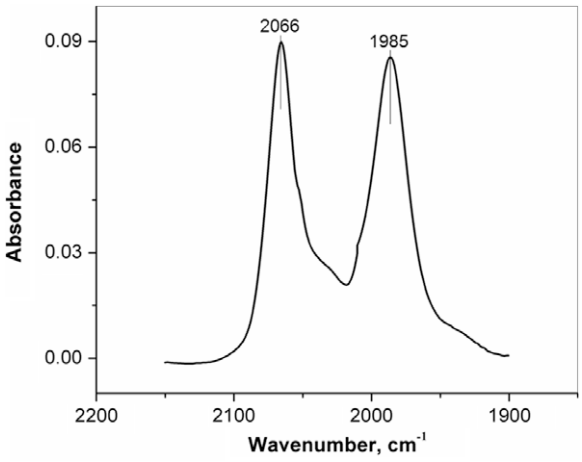

Fig. 7. IR spectrum characterizing the catalyst prepared by the reaction of $Ir(C_2H_4)_2(acac)$ with highly dehydroxylated MgO after ethene hydrogenation catalysis (under conditions stated in the text) for 2 h in a flow reactor followed by injection of a pulse of 10 vol% CO in helium (5 mL) into helium flowing at atmospheric pressure at a rate of 100 mL/min (after flow of helium for 1 h). The spectrum was recorded after the gas-phase CO had been purged from the flow system, as shown by mass spectrometric analyses of the product stream.

4.4.2. STEM evidence of site-isolated iridium complexes

The spectroscopic characterization of the used catalyst demonstrates that the nuclearity of iridium complex catalyst did not change significantly during the operation. However, it is known that iridium, like other group-8 metals, is characterized by a tendency to be reduced and aggregated into clusters and ultimately into metallic particles [26]. The STEM images of the used catalyst demonstrate that most of the iridium remained as site-isolated mononuclear species, but these images also provide evidence of the first steps of the process of cluster formation, as follows: the STEM images (Fig. 8) obtained for the MgO-supported iridium catalyst after it had functioned for 2 h at steady state (as demonstrated by mass spectra of the product stream) under the conditions stated above show that the bright scattering centers representing individual Ir atoms on MgO were still present. Thus, we infer that site-isolated mononuclear iridium complexes were still present on the support. However, the images also demonstrate the presence of a few iridium clusters consisting of only 2–4 atoms each (with the shortest Ir–Ir distances ranging from 2.7 to 3.8 Å) present together with the mononuclear iridium species (Fig. 8). The data are not sufficient to provide evidence of bonds between the Ir atoms in all of these clusters; however, the Ir–Ir distance of 2.7 Å characterizing some of these structures is short enough to be consistent with Ir–Ir bonds; this is a typical bonding distance in small iridium clusters [26]. Thus, these images appear to demonstrate the very first stages of cluster formation from the supported iridium complexes. The cluster formation may have been induced by the reactive atmosphere in the catalytic reactor, but we do not fully exclude the possibility of some beam damage during the scan of the sample.

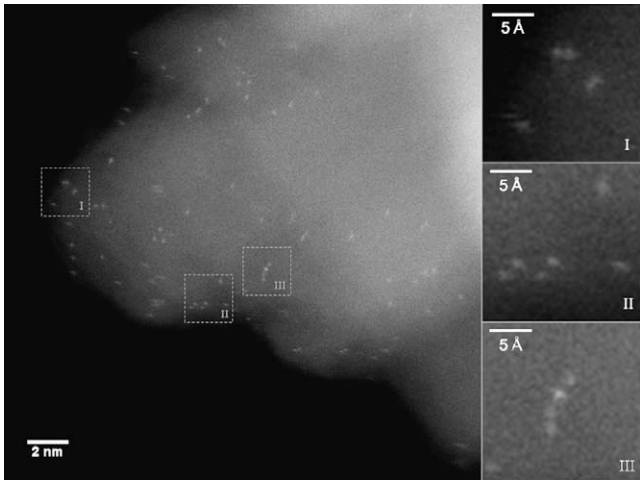

Fig. 8. High-angle annular dark-field (*Z*-contrast) image characterizing highly dehydroxylated MgO-supported iridium complex catalyst after use for ethene hydrogenation under the conditions stated in the text. The catalyst had functioned for 2 h in the flow reactor and was treated in flowing helium for 1 h before recording of the image. The image shows individual Ir atoms as bright scattering centers together with a few clusters consisting of 2–4 Ir atoms as shown in close-up images I, II, and III.

The data are not sufficient to determine a quantitative estimate of the fraction of the Ir atoms that might be present in clusters, but the qualitative result is clear: the iridium was predominantly present in site-isolated mononuclear iridium complexes in the used catalyst.

5. Discussion

5.1. Site-isolation of supported iridium complexes

Fundamental understanding of catalysis by supported metal complexes requires a detailed understanding of their structures and how they change during catalysis. Such a depth of understanding has not often been attainable, because the available spectroscopic techniques provide only average structural information, and the available microscopic techniques have lacked the resolution necessary to determine the nuclearity of metal-containing species as small as single-metal-atom species.

The images presented here show that STEM—under favorable circumstances—can determine the nuclearity even of such small species, and specifically can determine whether the metal complexes are truly site-isolated and whether they are present in the absence of metal clusters, which are known to form facilely when the metals are of group 8.

Observation of single metal atoms on a support by STEM is not new; there are examples of STEM images showing isolated individual metal atoms [20], together with metal clusters ranging in nuclearity from a few atoms to thousands of atoms, as shown, for example, in reports of iron oxide-supported gold catalysts [30], of TiO_2-supported gold catalysts [31], and of Al_2O_3-supported palladium catalysts [19].

But our images are the first to demonstrate the site-isolation of supported metal complexes in the absence of any higher-nuclearity metal species. The EXAFS and IR results complement the STEM results and provide evidence of the ligands on the iridium. We stress that the images had to be recorded quickly to avoid changes in the structures of the supported species by the electron beam.

5.2. Degree of uniformity of supported iridium complexes

STEM images characterizing the sample prepared by the reaction of $Ir(C_2H_4)_2(acac)$ with MgO clearly illustrate the site-isolation of the iridium complexes. However, the broad ν_{CO} bands (with fwhm values of approximately 26 cm^{-1}) characterizing the species formed by exchange of π-bonded ethene ligands with CO indicate that the degree of uniformity of these iridium complexes is not nearly as great as that of the analogous iridium complexes supported on dealuminated zeolite [3]. Therefore, we conclude that even as highly crystalline a support as our highly dehydroxylated MgO does not meet a high standard of uniformity as a support; the zeolite is far superior in this regard [3,25].

5.3. Reactivity of supported iridium complexes

The analogous zeolite-supported iridium complexes [3] were found to be approximately 15 times more active for ethene hydrogenation than our MgO-supported sample under the same conditions. Although the EXAFS and IR data indicate that MgO- and dealuminated HY zeolite-supported iridium complexes [3] have closely similar structures (with the anchored species, before catalysis, identified as $Ir(C_2H_4)_2$), their catalytic activities are significantly different. We infer that the different activities are attributable to differences in the ligands bonded to the metals—and the supports are ligands [17,32–34].

The differences in the ligand environments of the MgO- and zeolite-supported samples are confirmed by a comparison of the split between the symmetric and antisymmetric ν_{CO} bands of the complexes formed by the treatments of the samples with CO [35,36]. The split characterizing the MgO-supported complex (calculated as 81 cm^{-1} for ν_{CO} bands of 2066 and 1985 cm^{-1}, Fig. 5) is higher than that characterizing the zeolite-supported complex (calculated as 70 cm^{-1} for ν_{CO} bands of 2108 and 2038 cm^{-1} [3]). The greater split indicates stronger backbonding between the metal and the CO, thus a higher electron density on the metal [35,36]. Higher electron density on the Ir atoms in the MgO-supported complexes corresponds to a weaker bonding of reactants (e.g., ethene) to the metal as reflected by the υ_{CH} bands of the π-bonded ethene present in the unused iridium complexes on these supports: the frequency is centered at 3021 cm^{-1} for π-bonded ethene coordinated to zeolite-supported iridium complexes [3] and at 3034 cm^{-1} for π-bonded ethene coordinated to MgO-supported iridium complexes. We infer that the bonding strength between the iridium and the reactants is closer to the optimum for ethene hydrogenation to occur at high rates [37] in the zeolite-supported complexes than that in the MgO-supported complexes, but without more information about the reaction intermediates and mechanism we cannot provide further insight into the catalyst comparison.

Moreover, isostructural MgO-supported rhodium complexes (with the anchored species, before catalysis, identified as $Rh(C_2H_4)_2$) were found to have an activity approximately 3 times greater than that of the iridium complexes on the same support [6]. A similar trend in activity differences between rhodium and iridium clusters was reported [32–34,37,38]; Argo et al. [32–34] showed that MgO-supported Rh_6 clusters are more active than MgO-supported Ir_6 clusters for ethene hydrogenation in the presence of H_2 at 330 mbar and C_2H_4 at 130 mbar and 0 °C.

5.4. Identification of catalytically active sites

Although our IR and EXAFS results do not provide evidence of a substantial number of iridium clusters after the ethene hydrogenation reaction, the STEM images of the used catalyst (Fig. 8) indicate a few clusters consisting of only 2–3 Ir atoms each, indicating that the cluster formation had just started. Earlier results characterizing zeolite-supported mononuclear iridium complexes [3] and clusters [32–34] indicate that both mononuclear iridium complexes and iridium clusters are catalytically active for ethene hydrogenation, with the activities being roughly the same [39]. Thus, we infer that the catalytically predominant species in our catalyst were the mononuclear iridium complexes, even at the end of the flow-reactor experiment, as indicated by the (average) information provided by the spectroscopic techniques.

The STEM images presented herein show the very earliest stages of aggregation of the iridium, illustrating the unique value of STEM, resolving even the smallest metal species present in the catalyst and thus providing potentially crucial detailed understanding of supported metal catalysts, which our spectroscopic techniques are not sensitive enough to detect. Combining this unique capability of STEM with the capabilities of the spectroscopic techniques provides excellent opportunities for elucidating the separate roles of metal complexes and metal clusters in catalysis, by monitoring the structures present with various feed compositions and by correlating the structures with the catalytic properties.

6. Conclusions

Mononuclear iridium complexes with ethene ligands were prepared by the reaction of $Ir(C_2H_4)_2(acac)$ with highly dehydroxylated MgO. STEM images demonstrate the site-isolation of these iridium complexes, which were initially present in the absence of any iridium clusters or particles. Probing the structure of the supported iridium complexes with CO (leading to the formation of $Ir(CO)_2$ species) and determination of ν_{CO} IR spectra showed that the supported iridium complexes had a lower degree of uniformity than their zeolite-supported analogues (reported previously [3]). STEM images of the ethene hydrogenation catalyst after it had functioned in a flow reactor for 2 h showed that the mononuclear complexes were still the predominant species, in agreement with the EXAFS and IR results characterizing the used catalyst.

Acknowledgments

This research was supported by the US Department of Energy (DOE) (A.U., Grant No. DE-FG02-04ER15600) and by the National Science Foundation (NSF) (V.O., Grant No. CTS-0500511). We acknowledge beam time and the support of the DOE Division of Materials Sciences for its role in the operation and development of beamline X-18B at the National Synchrotron Light Source. We further acknowledge the Stanford Synchrotron Radiation Laboratory, operated by Stanford University for the US Department of Energy, Office of Science, Basic Energy Science, for access to beam time on beamline 2-3. We thank the beamline staffs at both facilities for their assistance. The STEM images were acquired at Oak Ridge National Laboratory's Shared Research Equipment (SHaRE) User Facility, supported by the Division of Scientific User Facilities, Office of Science, Basic Energy Science, DOE.

Appendix A. Supplementary material

Data characterizing catalyst performance including mass spectrometric data showing the catalytic formation of ethane when CO pulses were introduced into the IR cell containing the catalyst. Supplementary data associated with this article can be found, in the online version, at doi:10.1016/j.jcat.2009.11.017.

References

[1] G.G. Hlatky, Chem. Rev. 100 (2000) 1347.
[2] V.A. Bhirud, A. Uzun, P.W. Kletnieks, R. Craciun, J.F. Haw, D.A. Dixon, M.M. Olmstead, B.C. Gates, J. Organomet. Chem. 692 (2007) 2107.
[3] A. Uzun, V.A. Bhirud, P.W. Kletnieks, J.F. Haw, B.C. Gates, J. Phys. Chem. C 111 (2007) 15064.
[4] A. Uzun, V. Ortalan, N.D. Browning, B.C. Gates, Chem. Commun. (2009) 4657.
[5] H. Niu, Q. Yang, K. Tang, Y. Xie, Micropor. Mesopor. Mater. 96 (2006) 428.
[6] V.A. Bhirud, J.O. Ehresmann, P.W. Kletnieks, J.F. Haw, B.C. Gates, Langmuir 22 (2006) 490.
[7] R.E. Jentoft, S.E. Deutsch, B.C. Gates, Rev. Sci. Instrum. 67 (1996) 2111.
[8] J.F. Odzak, A.M. Argo, F.S. Lai, B.C. Gates, K. Pandya, L. Feraria, Rev. Sci. Instrum. 72 (2001) 3943.
[9] M.J. Newville, Synchotron Rad. 8 (2001) 322.
[10] M. Vaarkamp, J.C. Linders, D.C. Koningsberger, Physica B 209 (1995) 159.
[11] P.S. Kirlin, F.B.M. van Zon, D.C. Koningsberger, B.C. Gates, J. Phys. Chem. B 94 (1990) 8439.
[12] J.B.A.D. van Zon, D.C. Koningsberger, H.F.J. van't Blik, D.E. Sayers, J. Chem. Phys. 82 (1985) 5742.
[13] J. Guzman, B.C. Gates, J. Catal. 226 (2004) 111.

[14] S.I. Zabinsky, J.J. Rehr, A. Ankudinov, R.C. Albers, M. Eller, Phys. Rev. B. 52 (1995) 2995.
[15] J. Guzman, B.G. Anderson, C.P. Vinod, K. Ramesh, J.W. Niemantsverdriet, B.C. Gates, Langmuir 21 (2005) 3675.
[16] F.W. Lytle, D.E. Sayers, E.A. Stern, Physica B 158 (1989) 701.
[17] J. Guzman, B.C. Gates, Dalton Trans. (2003) 3303.
[18] W.D. Pyrz, D.J. Buttrey, Langmuir 24 (2008) 11350.
[19] S.F.J. Hackett, R.M. Brydson, M.H. Gaas, I. Harvey, A.D. Newman, K. Wilson, A.F. Lee, Angew. Chem. Int. Ed. 46 (2007) 8593.
[20] A. Uzun, V. Ortalan, Y. Hao, N.D. Browning, B.C. Gates, J. Phys. Chem. C 113 (2009) 16847.
[21] A. Uzun, V. Ortalan, Y. Hao, N.D. Browning, B.C. Gates, ACS Nano 3 (2009) 3691.
[22] I. Burkhart, D. Gutschick, H. Landsmesser, H. Miessner, in: P.A. Jacobs (Ed.), Zeolite Chemistry and Catalysis, Elsevier, Amsterdam, 1991, p. 215.
[23] F. Solymosi, E. Novak, A. Molnar, J. Phys. Chem. 94 (1990) 7250.
[24] M. Mihaylov, E. Ivanova, F. Thibault-Starzyk, M. Daturi, L. Dimitrov, K. Hadjiivanov, J. Phys. Chem. B. 110 (2006) 10383.
[25] H. Miessner, I. Burkhardt, D. Gutschick, A. Zecchina, C. Morterra, G. Spoto, J. Chem. Soc. Faraday Trans. 85 (1989) 2113.
[26] A. Uzun, B.C. Gates, Angew. Chem. Int. Ed. 47 (2008) 9245.
[27] B.A. Morrow, Can. J. Chem. 48 (1970) 2192.
[28] H.E. Newell, M.R.S. McCoustra, M.A. Chesters, C. De La Cruz, J. Chem. Soc. Faraday Trans. 94 (1998) 3695.
[29] J.-D. Grundwaldt, P. Kappen, L. Basini, B.S. Clausen, Catal. Lett. 78 (2002) 13.
[30] A.A. Herzing, C.J. Kiely, A.F. Carley, P. Landon, G.J. Hutchings, Science 321 (2008) 1331.
[31] W. Yan, B. Chen, S.M. Mahurin, V. Schwartz, D.R. Mullins, A.R. Lupini, S.J. Pennycook, S. Dai, S.H. Overbury, J. Phys. Chem. B 109 (2005) 10676.
[32] A.M. Argo, J.F. Odzak, F.S. Lai, B.C. Gates, Nature 415 (2002) 623.
[33] A.M. Argo, B.C. Gates, J. Phys. Chem. B 107 (2003) 5519.
[34] A.M. Argo, J.F. Odzak, B.C. Gates, J. Am. Chem. Soc. 125 (2003) 7107.
[35] K. Hadjiivanov, H. Knözinger, Surf. Sci. 603 (2009) 1629.
[36] K. Hadjiivanov, G. Vayssilov, Adv. Catal. 47 (2002) 307.
[37] S.B. Mohsin, M. Trenary, H.J. Robota, J. Phys. Chem. 95 (1991) 6657.
[38] G.C.A. Schuit, L.L. van Reijen, Adv. Catal. 10 (1958) 242.
[39] A. Uzun, B.C. Gates, J. Am. Chem. Soc. 131 (2009) 15887.